

THE SOLAR MASS-EJECTION IMAGER (SMEI) MISSION

B. V. JACKSON¹, A. BUFFINGTON¹, P. P. HICK¹, R. C. ALTROCK², S. FIGUEROA²,
 P. E. HOLLADAY², J. C. JOHNSTON², S. W. KAHLER², J. B. MOZER², S. PRICE²,
 R. R. RADICK², R. SAGALYN², D. SINCLAIR², G. M. SIMNETT³, C. J. EYLES³,
 M. P. COOKE³, S. J. TAPPIN³, T. KUCHAR⁴, D. MIZUNO⁴, D. F. WEBB⁴,
 P. A. ANDERSON⁵, S. L. KEIL⁶, R. E. GOLD⁷ and N. R. WALTHAM⁸

¹*Center for Astrophysics and Space Sciences, University of California at San Diego,
 La Jolla, CA, U.S.A.*

(e-mail: bvjackson@ucsd.edu)

²*Air Force Research Laboratory/Space Vehicles Directorate (AFRL/VS), Hanscom AFB, MA, U.S.A.*

³*School of Physics and Space Research, University of Birmingham, U.K.*

⁴*ISR, Boston College, Chestnut Hill, MA, U.S.A.*

⁵*Boston University, Boston, MA, U.S.A.*

⁶*National Solar Observatory, Sunspot, NM, U.S.A.*

⁷*Applied Physics Laboratory, Johns Hopkins University, Laurel, MD, U.S.A.*

⁸*Space Science Department, Rutherford-Appleton Laboratory, Chilton, U.K.*

(Received 25 February 2004; accepted 4 June 2004)

Abstract. We have launched into near-Earth orbit a solar mass-ejection imager (SMEI) that is capable of measuring sunlight Thomson-scattered from heliospheric electrons from elongations to as close as 18° to greater than 90° from the Sun. SMEI is designed to observe time-varying heliospheric brightness of objects such as coronal mass ejections, co-rotating structures and shock waves. The instrument evolved from the heliospheric imaging capability demonstrated by the zodiacal light photometers of the *Helios* spacecraft. A near-Earth imager can provide up to three days warning of the arrival of a mass ejection from the Sun. In combination with other imaging instruments in deep space, or alone by making some simple assumptions about the outward flow of the solar wind, SMEI can provide a three-dimensional reconstruction of the surrounding heliospheric density structures.

1. Introduction

The solar mass ejection imager (SMEI) (Eyles *et al.*, 2003) was launched early on 6 January 2003 into a Sun-synchronous polar orbit from Vandenberg Air Force Base (Figure 1). The Coriolis spacecraft (Figure 2) has two instruments: an all sky imager, SMEI, and a rotating radiometer instrument, *Windsat*, intended to measure ocean winds (Gaiser, 1999).

SMEI (Keil *et al.*, 1996; Jackson *et al.*, 1997, and references therein) is designed to map large-scale variations in heliospheric electron densities from Earth orbit by observing Thomson-scattered sunlight from within the heliospheric volume. Conceived as an all-sky coronagraph (Jackson *et al.*, 1989) SMEI views the outward flow of density structures in the solar atmosphere. These include solar coronal mass ejections (CMEs), co-rotating structures (streamers), and other solar wind density



Figure 1. Titan II launch of the Coriolis spacecraft on 6 January 2003 with the SMEI instrument on board.

enhancements, or depletions such as the density variations behind shock waves. SMEI is primarily intended to demonstrate the feasibility of forecasting the arrivals of these heliospheric structures at Earth; these normally take two to five days to travel 1 AU from the Sun. To achieve this, SMEI is operated as a differential photometer with unprecedented accuracy. The instrument may be regarded as a successor to the zodiacal-light photometers (Leinert *et al.*, 1975) of the twin *Helios* spacecraft and the heliospheric remote sensing capability demonstrated by this instrument (Jackson, 1985). Such analyses make use of *in situ* solar wind data from the vicinity of the imager and extends these observations to the surrounding environment and back to the Sun. Analyses of *Helios* data (Jackson and Hick, 2002) show that the three-dimensional location of these heliospheric density structures can be determined using tomographic modeling techniques that estimate their distance in each direction by using their line-of-sight rearrangement and change in brightness caused by outward solar wind flow.

This article discusses the design and mission considerations inherent in the construction and launch of the SMEI instrument. Section 2 is a history of the SMEI instrument design and development. Section 3 gives the signal levels expected from various heliospheric structures as derived from *Helios* spacecraft photometer



Figure 2. Coriolis spacecraft with the solar mass-ejection imager (SMEI) instrument on board prior to Vandenberg launch. Three instrument camera baffles (circled in red) are seen on the lower portion of the spacecraft.

data and first-principle analyses. Section 4 describes the data handling analysis designed and being implemented to deal with SMEI data. Section 5 describes a variety of background light sources that must either be removed or alternatively can be scientifically studied by SMEI. Conclusions are presented in the last section.

2. History of SMEI Design and Development

Global remote sensing of heliospheric structures has existed for a long time using ground-based metric radio wave interplanetary scintillation (IPS) analyses. The technique pioneered in Cambridge, UK, by A. Hewish and his associates (Hewish, Scott, and Wills, 1964) shows that data from a single large phased array measure different heliospheric structures as they move outward from the Sun (Gapper *et al.*, 1982). The most complete IPS measurements of this type have been interpreted to show that CMEs are not a dominant part of the interplanetary medium and that

co-rotating processes provide a more fundamental role in organizing heliospheric structure (Hewish and Bravo, 1986). In the early 1970s researchers at the University of California at San Diego used a system of three scintillation arrays (Coles and Kaufman, 1978) to derive solar wind velocities by watching the intensity scintillation pattern cross the surface of the Earth. These studies and observations are now being pursued by the STELab facility in Japan (Kojima and Kakinuma, 1990), and help provide ground-truth confirmation when compared with SMEI remote sensing observations, to locate and define heliospheric structures.

The relationship between scintillation intensity and the amount of small-scale density inhomogeneities in the solar wind has been explored in numerous journal articles (Coles and Kaufmann, 1978; Ananthakrishnan, Coles, and Kaufman, 1980). This relationship depends on the radio frequency used, radio source sizes, their numbers and placement relative to the Sun, and the numbers and line-of-sight locations of the small-scale (10–200 km) inhomogeneities. Although scintillation intensity is usually positively correlated to heliospheric bulk density (larger scintillation levels indicate greater densities), the relationship is not linear. Thus, it is difficult and less direct to determine the more fundamental heliospheric bulk density parameter, and whether CMEs dominate the inner heliosphere, using IPS data. With this incentive for monitoring heliospheric density structure in a more direct way than the IPS technique, the idea was initiated for a coronagraph that measures to large solar elongations (solar angular distances) in Thomson-scattered light.

The corona and heliosphere are optically thin to visible light outward from within a few minutes of arc of the solar limb. For ground-based observations mesospheric air glow is several factors of ten larger than heliospheric signals at even the darkest sites and is mottled on angular scales down to a few degrees and with variations on time scales less than an hour (Garcia, Taylor, and Kelley, 1997; James *et al.*, 1997). As a consequence, mesospheric air glow effectively limits ground-based Thomson scattering observations to elongations within a few solar radii of the Sun, even with the best observations obtained by high-flying aircraft during solar eclipses (Chapman, 1979). Thus, the only practical location for an instrument such as SMEI is in space.

The twin *Helios* spacecraft, launched in December 1974 (*Helios 1*) and January 1976 (*Helios 2*), each contained three zodiacal-light photometers which were intended to remotely measure the distribution of dust in the interplanetary medium between the Sun and the Earth (Leinert *et al.*, 1975; Leinert, Link, and Salm, 1981). The *Helios* spacecraft orbited the Sun from 0.3 to 1 AU with a six-month period, and their photometers viewed heliospheric structures from a non-Earth location with low spatial resolution. The time cadence of observations was about 5 h between the same combination of color and polarization filters for a given photometer. These photometers also measured brightness variations of interplanetary electron density produced by Thomson scattering from large-scale structures (Richter, Leinert, and Planck, 1982). They first described use of these data to detect and follow plasma ejections in Thomson scattering brightness out to 90° solar

elongation. Subsequently, Jackson (1985) used these data to study characteristics of mass ejections and trace their motion outward from the Sun into the anti-solar hemisphere. Jackson (1991) also used these data to study the longer-lasting co-rotating regions in the solar wind.

Building on this instrumentation and these ideas we have designed SMEI to view nearly the entire sky in visual light during each 102-min Earth orbit, and to map large-scale variations in heliospheric electron densities. SMEI provides roughly an order of magnitude improved angular and photometric resolution compared with *Helios*, and a three-fold faster cadence for full-sky maps. Designed for deployment on the *Wind* spacecraft, SMEI was initially conceived to operate on a rapidly-rotating satellite in deep space (Jackson *et al.*, 1989). In this configuration the SMEI detectors would have counted individual photons and integrated their totals over time much as the *Helios* photometers did. Since then, cooled, low-readout-noise CCD detectors have become available and are commonly flown in space. Accordingly, SMEI was redesigned for the Air Force Space Test Program P91-1 spacecraft. When resources proved unavailable to include the instrument on P91-1, SMEI was placed on hold until the University of Birmingham, UK, with the help of NASA funding, joined the effort with contributions of manpower and money starting in 1995.

The current SMEI instrument (Eyles *et al.*, 2003) is a joint international effort. Most features of the original P91-1 design concept were retained: the bulk of the SMEI hardware was designed, fabricated and qualified by the University of Birmingham. SMEI incorporates a CCD camera design from Rutherford–Appleton Laboratory (RAL). The University of California at San Diego (UCSD) designed, procured and tested the prototype and flight-model optics, and built and tested an early prototype baffle developed for the *Wind* spacecraft employing a proprietary Martin Black coating (Martin Marietta Company, 1977). Later, UCSD tested a prototype baffle built at the University of Birmingham and also the flight-model baffles (Buffington, Jackson, and Hick, 2002). UCSD photometrically certified the prototype and flight cameras for use on SMEI. The Air Force Research Laboratory (AFRL), Boston University, Boston College, the University of Birmingham, and UCSD have provided management of the SMEI development and, more recently, data processing and preparation of SMEI data products.

Coriolis was successfully launched on 6 January 2003 from Vandenberg AFB on board a Titan II booster. The spacecraft was inserted into an elliptical ($\sim 270 \times 830$ km) Sun-synchronous polar orbit. Spacecraft control after launch was performed from the Space and Missile Command Center in Albuquerque, NM. The first month of the mission (Launch and Early Operations, or L/EO) was devoted to bus and payload initialization and checkout, and circularization of the spacecraft orbit at an altitude of about 840 km. During the first three weeks of L/EO, SMEI was powered on and the basic functioning of the three cameras was verified. The baffle doors remained closed and the CCDs kept heated to $+30^\circ\text{C}$ to minimize deposition of volatiles from thruster firings and spacecraft outgassing. On 1 February 2003 the

TABLE I
Expected signal levels.

| Structure | Elongation (degrees) | Signal intensity (S10)* | Signal duration (days) |
|----------------------------|-------------------------|----------------------------|---------------------------|
| Bright CME | 60 | 2 | 1.5 |
| | 90 | 1 | 1.5 |
| Bright streamer | 60 | 2 | 1 |
| | 90 | 1 | 1 |
| Bright shock | 90 | 0.5–1 | ≤0.5 |
| Major unidentified | 60 | 3 | 2 |
| <i>In situ</i> fluctuation | 90 | 2 | 2 |
| Comet shock | 20 | 3–10 | – |

*Signal levels are given in units of “S10” which is the surface brightness equivalent to the flux of a single tenth magnitude solar-type star per square degree of sky.

SMEI baffle doors were opened, and one day later the CCD temperatures were reduced to their current operating levels.¹ In the final days of the L/EO period, SMEI obtained its first all sky maps.

3. SMEI Signal Levels and Data Requirements

Because the Sun is much brighter than the faint coronal structures we wish to detect, SMEI was designed to carefully control the stray light background to provide a photometric sky signal that does not vary significantly over the same time intervals as the heliospheric structures being measured. Table I gives estimates of the signal levels expected for various phenomena at 1 AU.

In the above table, the brightness for coronal mass ejections (CMEs) and for streamers was derived from structures traced outward using the Naval Research Laboratory’s SOLWIND coronagraph (Sheeley *et al.*, 1980), the High Altitude Observatory SMM coronagraph (MacQueen *et al.*, 1980), and the *Helios* photometers (Jackson, 1991).

Shock brightness was estimated from the *in situ* plasma density enhancements behind shocks observed from the *Helios* spacecraft. The values were adjusted to 1 AU by assuming their brightness decreases as R^{-3} from the locations where they were actually observed closer to the Sun (Jackson, 1986). The comet shock estimates are from Jackson and Benensohn (1990).

Thomson-scattered light must be separated from many other sources of diffuse light: background light from the Sun, Moon or Earth scattered into the SMEI field

¹The sunward-facing camera (Camera 3) did not achieve an operating temperature at the designed -30°C ; its temperature decreased to only about -3°C .

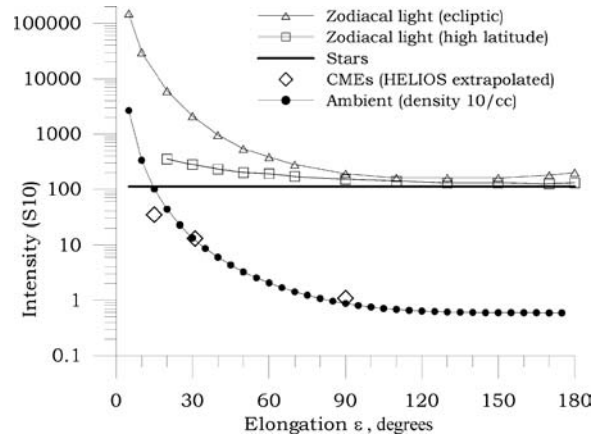


Figure 3. Surface brightness versus solar elongation for zodiacal and star light (Allen’s *Astrophysical Quantities*, 2000), and of expected CME brightness extrapolated from *Helios* measurements. A calculation of an ambient medium having a density of $10 \text{ e}^- \text{ cm}^{-3}$ at 1 AU and an inverse-square density dropoff with solar distance is also shown.

of view; zodiacal light; and starlight, either individually as bright point sources or collectively as a mottled contribution to the diffuse sky brightness. Figure 3 shows estimates of the brightness contributions from these signals expected at SMEI as a function of elongation from the Sun. The Sun is the equivalent of 4×10^{14} S10 units. A fundamental limit to diffuse-light photometry is set by photon counting statistics; a good instrument design reduces other noise sources to this level. This limit depends upon the optics and scanning configuration, spectral bandpass, and detector efficiency. Total detected photon count N (e.g., Jackson *et al.*, 1989) is:

$$\log_{10} N = 6.15 - 0.4m + \log_{10} A \cos \theta + \log_{10}(\Delta t), \quad (1)$$

where A is the aperture area (cm^2), θ the incident-light angle relative to the aperture normal, Δt the integration time (seconds), and m the brightness “magnitude” in a square degree evaluated for the instrument’s particular bandpass. Here, the constant 6.15 includes the bandpass efficiency for the combination of SMEI CCD and optics. For SMEI, the background sky brightness varies roughly over the range 60–6000 S10 units between the darkest sky and the ecliptic plane at a solar elongation of $\sim 20^\circ$. The aperture is approximately $1 \times 2 \text{ cm}$ with $A = 1.76 \text{ cm}^2$, and with $\Delta t = 4\text{s}$, approximately 1000 electrons are detected per S10. A given portion of sky is covered by a dozen or more frames in a single orbit, and a single-orbit photometric sky map combines roughly 1500 data frames from each of three cameras (see Eyles *et al.*, 2003).

The heliospheric sky brightness is large enough that CCD readout noise ($\sim 14 \text{ e}^-$ rms) is not a significant factor for the SMEI camera systems when operated at the appropriate temperature. The SMEI instrument has been developed around the use

of a cooled E2V CCD05-30-321A frame-transfer CCD chip, in part because this device was shown to have a satisfactory sub-pixel gradient response needed to reproduce stellar point images as they change position in the SMEI field of view (Buffington, Booth, and Hudson, 1991). To provide a reproducible photometric response with the extremely fast ($\sim f/1$) SMEI optics, unresolved point images occupy approximately 200 CCD pixels or about 1/2 square degree.

To ensure that square-degree sky locations are reproduced accurately on each orbit for the duration of heliospheric structure passage (hours to several days), the SMEI instrument requires that the response in this square degree from other sources of brightness be constant or slowly-varying to a fraction of one S10 unit. This is needed to separate heliospheric structure brightness variations from other sources of background light. Each square degree of sky contains an average of 120 S10 units of equivalent stellar signal (see Figure 3) and one star of eighth or brighter magnitude. Stellar background brightness, shown here as an average over the whole sky, varies significantly from the Milky Way to the galactic poles. Orbital motion sweeps the SMEI camera's narrow dimension over any given sidereal location in a minimum of approximately 50 s, and a sufficiently accurate value for stars must be recorded along with the background sky brightness despite this motion. In order that this and other bright background signals such as zodiacal light do not overwhelm the faint heliospheric signal, the differential photometric specification for these must be even better than required to eliminate stellar signals alone (see Figure 3) so that heliospheric structures are measured to a fraction of their intensities. Thus, a differential photometric specification for all signals incident on the SMEI focal plane at 90° elongation in one square degree of sky in a single camera passage has been set at 0.1%.²

The SMEI light baffles (Figure 4) are designed so that the SMEI photometric specification can be met provided the solar limb does not approach the edge of the field of view to within 18° and 27° in the camera field-of-view's narrow and wide dimensions, respectively. When the SMEI cameras point closer than this to the Sun, the above photometric specification is unlikely to be met (Buffington, Jackson, and Hick, 2002) because sunlight illuminates the Z3 edge and the inner portion of the baffle. This portion of the baffle is imaged out of focus onto the CCD beyond the SMEI $3^\circ \times 60^\circ$ field of view and when illuminated, as discovered on orbit, has sufficient brightness to saturate it with a 4 s exposure. The baffle must also reject sources of background light other than the Sun, including spacecraft appendages and instrumentation, and Earth shine. Having SMEI point away from Earth controls this latter source of background light, and having SMEI also point away from the rotating (30 rpm) *Windsat* antenna (Figure 2) controls this potentially

²Certain regions in the sky near bright stars, variable stars and planets exceed the 0.1% photometric specification. The brighter planets saturate a region of the CCD data frame near the planet. The Moon and stray light from it cause saturation of the CCD if the Moon is within 9° of the edge of the camera field of view.

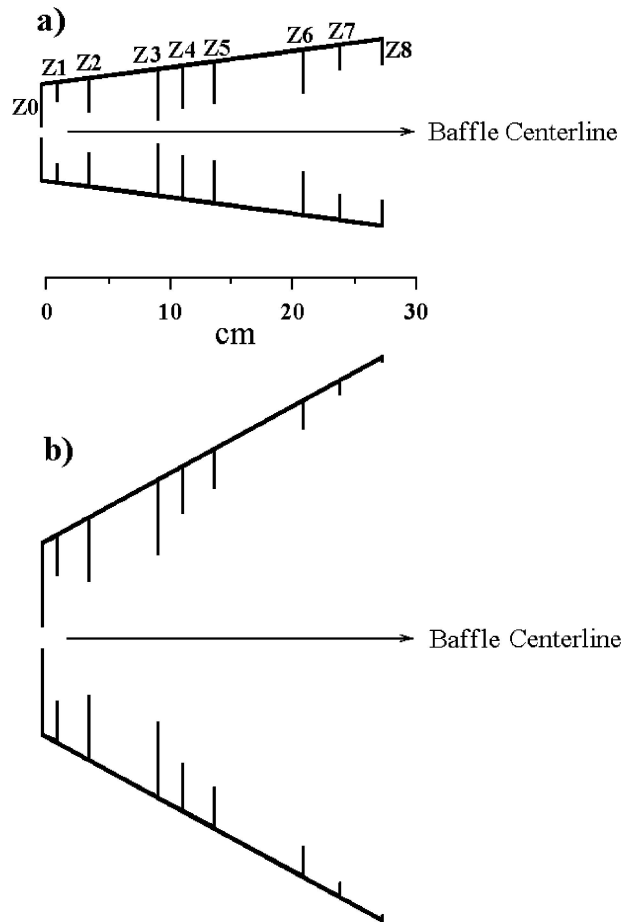


Figure 4. Schematic of SMEI baffle. The scale is in centimeters. Apertures are numbered Z0 to Z8 in advancing distance towards incident light along the baffle centerline. (a) Narrow dimension. (b) Wide dimension.

variable spacecraft light source. Figure 5 shows an artist's conception of the SMEI instrument in its polar orbit.

4. SMEI Data Operation and Analysis

The main goal of the SMEI mission, operating in conjunction with other programs, is the detection of solar mass ejections and forecast of their arrival at Earth. Although SMEI, like any white-light coronagraph, measures heliospheric Thomson-scattered light integrated along each line of sight, the full-sky sky view from SMEI requires that special care be taken to insure that the variations in brightness from these very

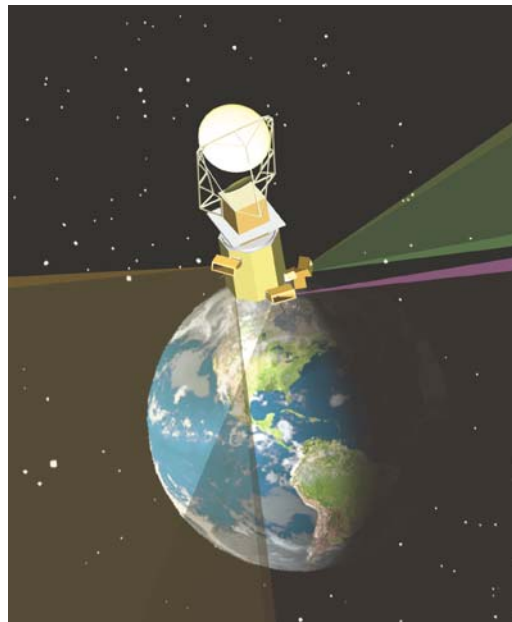


Figure 5. Schematic of SMEI in orbit. The spacecraft orbit is nearly circular at 840 km above the surface of the Earth with an inclination of 98° relative to the equatorial plane. SMEI looks outward from the Earth over an $\sim 180^\circ$ range of sky from three baffled cameras. The SMEI cameras and their fields of view as depicted are directed approximately 30° above the local horizontal to avoid both light from the Earth and sunlight reflecting from the rotating *Windsat* antenna (see also Figure 2).

faint signals are detectable over the whole field of view. To provide a composite heliospheric sky map, individual $3^\circ \times 60^\circ$ SMEI camera CCD data frames like those shown in Figure 6a must be combined to provide all-sky maps. The AFRL “first light” example of such a map is shown in Figure 6b. In these Hammer–Aitoff sky map projections the Sun is centered with ecliptic north at the top and solar east to the left. In a Hammer–Aitoff projection of the whole sky such as this, the area on the surface of the celestial sphere is preserved on the planar viewing surface. The map becomes more distorted towards its perimeter in order to preserve sky area over the image.

4.1. SMEI DATA ACCUMULATION

SMEI mission data (both camera and state of health data) are stored in a solid state recorder (SSR) aboard CORIOLIS until X-band downlink to the ground. The SMEI partition of the SSR was originally sized to hold 24 h of mission data before overwriting. However, part of the strategy for dealing with the hot camera 3 has been to operate that camera in a 2×2 pixel binning mode, rather than 4×4 . This has increased the data rate, such that SMEI now fills its SSR partition in about

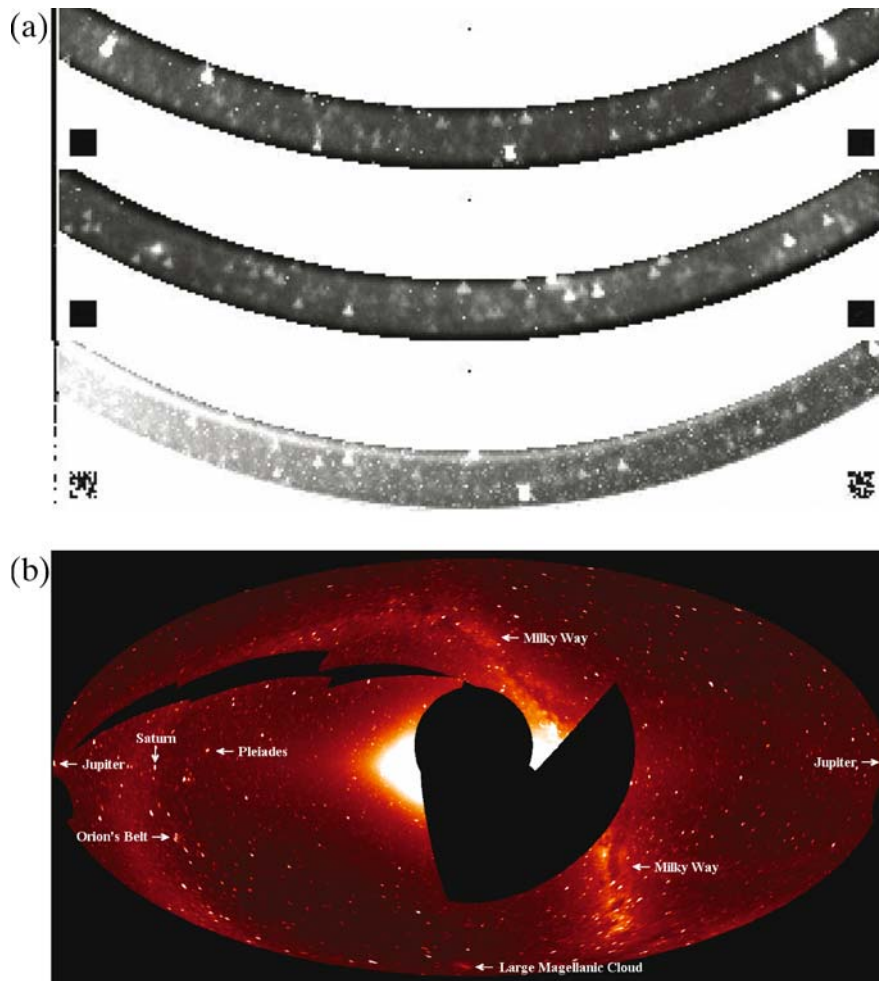


Figure 6. (a) SMEI $3^\circ \times 60^\circ$ data frames from each of the three cameras arranged in order from top to bottom, the one viewing farthest to the one viewing nearest the Sun. The Sun is located towards the left in each data frame. (b) A full orbit's worth of frames are registered onto a high-resolution sky map and together build a composite view of the sky over that orbit that can be projected as a sky map (here shown as a full-sky Hammer–Aitoff projection). Various bright features are labeled on the map. Blank areas are regions that were excluded from the composite view either because they were not accessible to the cameras during the orbit, were too close to the Sun and thus too bright, or were contaminated by Earth radiation-belt particle enhancements (the slash across the upper left of the sky map).

12 h. Typically, this does not result in any data loss unless downlink problems occur. X-band downlinks are scheduled, typically 6–8 per day, to ground stations in Alaska and Sweden operated by the Integrated Program Office of the National Polar-orbiting Operational Environmental Satellite System (NPOESS/IPO) and, over the first year of operation, to the Universal Space Network (USN). The data are sent

from the ground stations to the US Navy's Fleet Numerical Meteorological and Oceanographic Command (FNMOOC) in Monterey, CA, where they are temporarily stored and sent onward via commercial link to both AFRL at Hanscom AFB, MA and the National Solar Observatory in Sunspot, NM.

The telemetry data is received by the AFRL SMEI data processing center in the form of 522-word telemetry packets, each consisting of 10 words of header information and 512 words of SMEI data. These are read and processed by a routine that parses the SMEI data stream and outputs the data in a computer compatible format. The routine also performs quality checks on the data stream, decompresses the data using a Rice algorithm (lossless), and assigns an averaged set of spacecraft quaternions (spacecraft pointing coordinates derived from a star tracker) to each four-second frame header.

The resulting CCD frames data are distributed to the University of Birmingham, and UCSD via FTP so that SMEI team researchers at these sites can carry out quality checks on the raw data and use them for further interactive analysis. These CCD data frames provide the input to data processing by each group and in particular to AFRL for near real-time data processing.

4.2. SMEI DATA ANALYSIS

Two data analysis techniques have been devised, one at UCSD and another at AFRL, to provide composite sky maps from SMEI data frames. Appendices 1 and 2 provide detailed descriptions of these techniques; both are evolving as the requirements for SMEI data analysis become better understood. The techniques are similar, and carry out the following sequence of steps:

- Identify and remove corrupted data frames.
- Remove frames saturated by sunlight, moonlight, and bright planets.
- Remove or mitigate CCD blemishes such as "hot" pixels, and subtract the dark current and electronic pedestal offset. These latter are determined from data in the "covered" or empty columns in the CCD readout.
- Remove or reduce the effects of the Earth radiation belts, cosmic rays, and space debris.
- Correct for flat field variation in the CCD response and correct for optical geometric effects.
- Register and average frames onto a standard sky grid.
- Remove sidereal sky brightness and zodiacal light.
- Provide derivative data products for use in further analyses.

The first five items in the preceding list are applied to individual CCD data frames, while the final three apply to the later ensemble of a single SMEI orbit. These items are described in more detail in the following section.

4.2.1. *Individual Frame Conditioning – Hot Pixels, Cosmic Rays, and Space Debris*

CCD pixels that show abnormally high dark charge response, i.e., “hot pixels” are present in each CCD data frame. This source of unwanted CCD noise mimics cosmic ray hits (see below) in individual pixels, but remains at the same place on the CCD. Some of the algorithms designed to eliminate cosmic ray noise may also eliminate these hot pixels if they are not too numerous. However, hot pixels are generally hot by a prescribed amount, and if each pixel that is hot is known by location, then its effect can be directly subtracted from the data. SMEI camera shutters, designed to keep sunlight from falling directly onto the CCD (Eyles *et al.*, 2003) are closed every few weeks, and data taken during these intervals are used to calibrate the SMEI images. To do this a fixed pattern is subtracted from each CCD data frame determined from closed-shutter data taken from a time as near as possible to that of the original observation. There is a dependence of hot pixel value on CCD temperature, and thus varying CCD temperature can alter the effect of a given hot pixel such that its effect does not remain constant over time. This is especially a problem for the hottest pixels. This same hot pixel behavior with temperature is also noted in hot pixels that cycle between two or more hot states with time.

Hot “flipper” pixels are also present in the CCD. These pixels cycle between two or more states over periods of minutes to days. As with hot pixels, if these pixel locations are known and their states recognized, their effect can be removed partially on a pixel-to-pixel spatial scale by subtracting a pattern. The hot and flipper pixels become more numerous with time as the CCD suffers on-orbit radiation damage. The effects of flipper pixels are more evident if the CCD does not operate at its prescribed low temperature (-30°C). This problem especially affects SMEI Camera 3 (that points close to the Sun, operating from $\sim 3^{\circ}\text{C}$ to -10°C). Until careful mitigating steps are taken to alleviate this source of unwanted noise, the sky maps from this camera will have a higher than desired background noise from this effect. Cumulative energetic charged particle damage to CCD chips with time can be partially reduced by annealing the chip (heating the chip to temperatures well above the operating temperature). CCD annealing is routinely performed on several space missions, including the SOHO EIT and the Hubble WFPC2 (for the latter see Biretta and Lubin, 2002) and are now performed similarly on SMEI.

Each orbit of the Coriolis spacecraft passes through the Earth’s north and south auroral ovals, and some orbits pass through the South Atlantic Anomaly. In addition to the unwanted effect of contaminating SMEI image frames at these times, such exposures to high particle fluxes couple with the relatively exposed location of the SMEI Data Handling Unit (DHU) on the spacecraft to produce processor upsets at a rate of about two per month. Although readily cured by resetting the DHU processor, these upsets result in data loss.

Energetic charged particles can cause anomalies in individual data frames or sequences that affect the telemetry data packet output stream. These introduce half-transmitted or partial data frames into the data sequence and need to be searched for

in the incoming data stream and removed on a frame-by-frame basis from further consideration in the analysis.

In addition to the hot flipper pixels, SMEI data frames also contain energetic particle contamination that varies from orbit to orbit and with spacecraft location. Cosmic rays and trapped particles deposit widely varying energy in each CCD pixel they impact, and above some threshold that pixel no longer provides a meaningful photometric measurement. Two distinct types of trapped particle signals have been detected in SMEI data frames to date, a hard component of several hundred MeV protons and heavier nuclei, and a soft component, probably electrons. The hard component passes through the CCD detectors having penetrated the surrounding spacecraft structure without noticeable attenuation. These are uniformly distributed over the CCD and often appear as streaks along several pixels. The soft component is collimated by the camera baffles and optics and reaches the CCD after scattering from the SMEI primary mirror (see Eyles *et al.*, 2003). Closing the camera shutter decreases this soft particle component by about 90%. The soft and hard particle components occur at different geographic locations along the orbit; the soft component lasts for a few minutes as the spacecraft passes through the outside edges of each auroral oval, while the harder component lasts as long as 15 min when passing through the South Atlantic Anomaly.

The more particle hits present in a data frame, the fewer pixels remain useful to contribute to that orbit's sky map. At some level, especially in the middle of the South Atlantic Anomaly, these spurious signals overwhelm any algorithm that could remove their effects by using spatial and temporal filters. The fact that stellar signals move on the CCD from one frame to the next further complicates the situation. A threshold must be chosen above which these removal algorithms are overwhelmed and the entire frame must be discarded. This creates holes in a given orbit's sky map similar to the ones noted in Figure 6b. An aggressive cosmic-ray removal algorithm may fill in most of the sky area in a map such as in Figure 6b, but may also contribute photometric noise to heliospheric analysis if it wrongly identifies portions of bright stars moving over the CCD pixels as cosmic rays. If the optimum photometric response of stellar signals is to be preserved, then a lesser degree of cosmic ray removal may be desirable.

During a single orbit tens of satellites and space debris appear, distinct from the other types of SMEI signals, as streaked point objects present in one or sometimes several consecutive exposures. If allowed to remain in a sky map these will degrade overall SMEI photometric performance. Some automatic method is required to remove the effects of at least the brightest of these.

4.2.2. Flat Fielding

Once individual spatial defects such as those described above are removed from an individual SMEI data frame, flat-field corrections are applied so that the individual SMEI data frames will average together seamlessly. A small-scale flat-field correction is carried out by SMEI on-board processing. This is necessary, since the

camera frames are usually binned onboard into 4×4 pixel groups prior to telemetry. The small-scale flat-field corrections to the binned data are typically only a few tenths of a percent adjustment of the total response of a pixel, and in most cases leave unchanged the average response of a 4×4 binned group. Occasional larger corrections are made on sections of the CCD where light blockage is caused by a few dust particles on the CCD chip, mostly accumulated prior to flight. When the on-board small-scale flat-field correction table is applied, a “headroom” factor of 0.75 multiplies all responses to avoid exceeding the 16-bit limitation for telemetry data. SMEI has the option to modify these small-scale effects on a pixel-by-pixel basis on orbit if the modifications are not numerous and do not change too rapidly. A large-scale flat field correction is applied to SMEI data by ground-based data processing before the individual data frames are combined into a 0.1% photometric sky map. These were determined for each camera prior to flight to $\sim 1\%$ using exposures of a uniformly-illuminated white cloth, but in ongoing analysis must be refined roughly tenfold on-orbit, primarily to remove long term trends in the stellar background. A means of doing this has been devised by comparing sky maps that have occupied different locations from each CCD. When different locations on a chip systematically disagree with the mean from all locations of the chip, their response can be modified by a multiplicative factor to achieve the mean result. In this way the CCD large-scale flat-field can be refined as more data are used in the analysis until it reaches the requisite 0.1% differential photometric specification everywhere.

Although the viewing perspective $\cos \theta$ term in Equation 1 could be thought of as part of a “flat-field correction,” this is included separately and analytically since it is not caused by on-chip CCD response variations. Similarly, the per-pixel observed surface brightness increases toward the inside of the CCD-frame arcs seen for each camera in Figure 6a, and this is also adjusted analytically since it is a well-understood geometric effect unrelated to actual CCD response variations.

4.2.3. *Frame Registration onto a Standard Grid*

Once the above corrections have been applied, individual SMEI data frames are registered onto a standard sky grid so they can be combined and averaged to yield heliospheric sky map images in the desired viewing format such as Hammer–Aitoff or “fisheye” (Sub-Section 4.3.). The spacecraft quaternions locate the spacecraft pointing to within $\sim 0.01^\circ$, typically averaging 20 measurements throughout a 4 s exposure. Individual measurements are accurate enough to show the wobble impressed on SMEI by the rotating *Windsat* antenna ($< 0.05^\circ$), and to mark the Earth-centered rotating motion of the spacecraft with time during an exposure. Each camera has a fixed relationship between the spacecraft quaternion direction and its viewing orientation in the sky, and given that there is no change in this relationship, the averaged spacecraft quaternions then usually suffice to register each camera’s frame to the above $\sim 0.01^\circ$ accuracy, close to that required to preserve the SMEI photometric precision. However, in principle, for the finest pointing precision, there

are a sufficient number of stars in a data frame to register each to the final accuracy required ($\sim 0.004^\circ$ for 4×4 binned pixels). Some actual star-fitting technique may prove necessary to refine this registration if changes on orbit due to temperature or some other effect require it.

Both the UCSD (Appendix A) and AFRL (Appendix B) techniques are similar in that they produce sky maps by combining and averaging individual data frames onto a high resolution sidereal map. However, the techniques devised at UCSD and AFRL diverge significantly, since they address different ultimate uses of the maps. The AFRL technique, available soon after launch, has allowed an expedient presentation of SMEI data in the form of Hammer–Aitoff sky maps as in Figure 6b. These data have been presented in near-real time to the SMEI team and, when differenced from one orbit to the next or from an average of nearby orbits, show CMEs and allow their tracking. The UCSD technique instead is driven by the requirement that the composite sky maps be processed to as near the photometric limit as possible, and to retain the original SMEI data frame spatial resolution. In order to use SMEI sky maps to observe both background heliospheric structures that take several days to pass a given sky coordinate as well as rapidly-moving features, these maps must retain as long a constant temporal base as possible. The main differences between these lies in the choice and fineness of the sidereal coordinate grid on to which the individual CCD camera frames are combined, and the AFRL “symmetrization” of the data, which reduces the angular resolution.

4.2.4. *Sidereal Sky and Zodiacal Light Background Removal*

The light from the sidereal sky (stars, the Milky Way, bright nebulae and galaxies) is much brighter than the variable Thomson-scattered signal we wish to detect (Figure 3). Thus, these brightness contributions must be subtracted from orbit-to-orbit SMEI sky maps. The simplest way to remove this background is either by subtracting orbits adjacent in time (then only the heliospheric change in signal in adjacent orbits remains) or by subtracting an average sidereal orbit map that combines several adjacent orbits together (Figure 7). To first order, SMEI instrument changes and sidereal background changes combined are small enough that differences from the average over a few days do not degrade overall SMEI performance beyond the photometric limit (shown for a difference from an average of sky maps in Figure 8). For time intervals longer than a few days, the Earth’s orbital motion around the Sun slowly re-orientes the asymmetrical stellar images (Figure 9) such that unresolved bright stars no longer subtract from one another properly and this adds significant noise to the resulting heliospheric map.

The zodiacal light contributes significantly to the sky background (Figure 3). However, this signal does not vary much relative to solar elongation or position angle, and it can be separated from the rapidly-changing solar heliospheric component. We eliminate this signal (to first order) by subtracting a simple Sun-centered model that approximates the angular shape of the brightness; this is one of the signals we expect to refine significantly with the SMEI data. In order to provide the

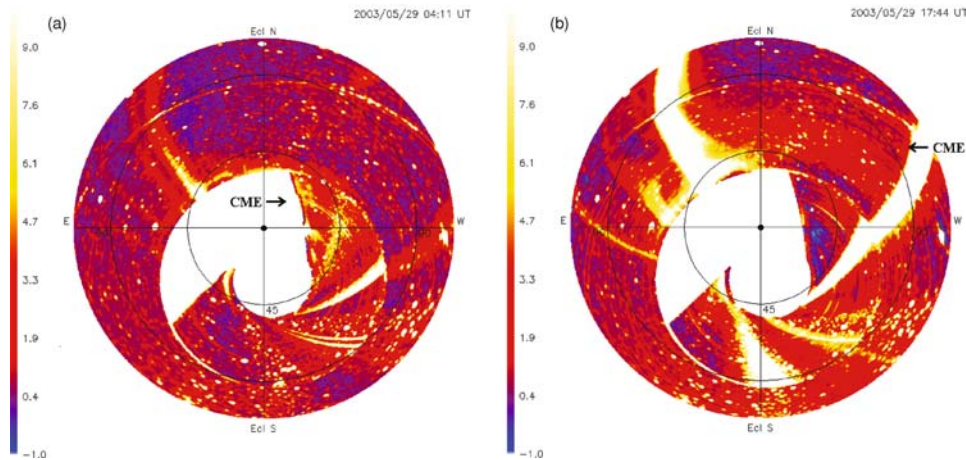


Figure 7. Shown are “fisheye” 102-min composite sky maps from two orbits of data differenced from an 8-orbit average for SMEI Cameras 1 and 2 data with CCD pixels binned using normal science mode operation (4×4) and for SMEI Camera 3 data binned 2×2 . The differences show a CME (arrow) that was observed on 28 May 2003 to surround the Sun in the LASCO data. The brightness scale is in ADU. The blank area in the middle of the map is the location that cannot be accessed at this time of the year where Camera 3 looks too close to the Sun. These data have been averaged into 1° bins using a Gaussian filter that extends circularly in spherical angle from each location on the map. Circles on the map are Sun-centered at 45° and 90° elongation; ecliptic north is at the top. The beginning time of the data that produces the sky map is indicated to the upper right of the map, and for this display proceeds clockwise around map center from the southernmost point of the map. The oblong points scattered throughout the map are mostly variable stars that have changed brightness relative to the subtracted minimum. The techniques used to provide these sky maps are outlined in Appendix A. (a) The outer edge of the CME is at about 45° elongation due north and encircles the Sun from northwest to south reaching $\sim 60^\circ$ elongation due west. (b) The CME has progressed farther and its bright portions have reached beyond 90° (at least 1 AU) to the northeast and south completely encircling the Sun and raising the general background level over nearly the entire sky. The blank approximately radial region to the solar northeast in this map is a bright band of auroral light where SMEI passes through the Earth’s northern auroral oval. The blank radial region to the solar northwest is a location where energetic charged particles were too numerous to allow the desired photometric performance as SMEI passed through the South Atlantic Anomaly.

more accurate photometric SMEI sky maps required as the input to tomographic analyses, secondary effects of this signal that change with the Earth’s orbital motion around the Sun can be removed by a high-pass temporal filter such as is done to analyze *Helios* photometer data (Jackson and Hick, 2002).

4.3. HELIOSPHERIC PLASMA BRIGHTNESS

With careful removal of the above-described blemishes, starlight and zodiacal light, SMEI can detect and track CME disturbances to beyond 1 AU (Figure 7) (see Tappin *et al.*, 2004). Over the first year of SMEI operation, analysis using SMEI difference

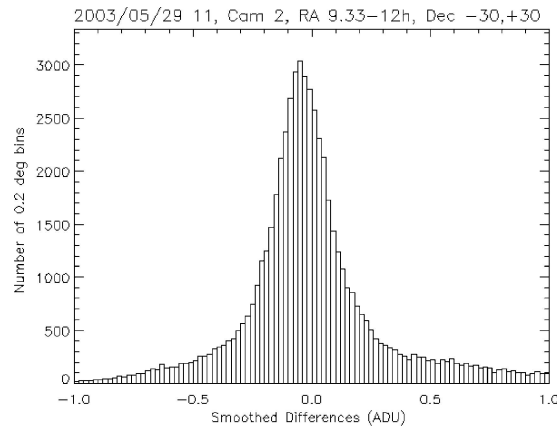


Figure 8. Histogram of a 40° by 60° portion of the sky map in Figure 7a from right ascension 9 h 20 min and declination -30° respectively (to the solar southeast centered on an elongation 90° from the Sun). The response on the ordinate is in Analog to Digital Units (ADU). Ground-based and SMEI on-orbit “G-type” stellar subtractions give a preliminary calibration of this histogram of $1 \text{ S10} \approx 0.55 \text{ ADU}$, and thus the mean square difference for the portion of the sky map that makes up the histogram is $\sim 0.2 \text{ S10}$.

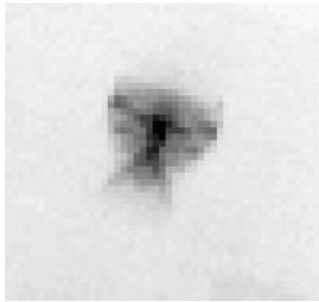


Figure 9. Shown is a typical unresolved SMEI stellar image (β Draco, $M_v = 2.79$). The image shape is produced by the fast ($\sim f/1$ focal ratio) SMEI optics which spreads the light from a point source as uniformly as possible over ~ 200 CCD pixels. The scan direction for the SMEI instrument is approximately from top to bottom in this image.

imaging techniques revealed more than 100 of these CME-like disturbances. Many of these were first observed near the Sun by the SOHO Large-Angle Spectroscopic Coronagraph (LASCO) experiment (Brueckner *et al.*, 1995). A handful of these CMEs remained observable at elongations greater than 90° from the Sun. Using SMEI to determine whether a CME is headed toward Earth, away from Earth, or to one side, is described by Jackson, Gold, and Altrock (1991) or Webb, Johnston, and Radick (2002). However, a major requirement for any Earth-based forecast instrument is that it should also allow determination of the solar distance of heliospheric structures. How SMEI data can provide this distance has been shown in a

rudimentary way from interplanetary scintillation (IPS) analyses by Gapper *et al.* (1982) and Behannon, Burlaga, and Hewish (1991). In these analyses the shapes of heliospheric structures over time are viewed to determine whether they loom bigger on either side of the Sun as they arise from it, or whether they persist to the east of the Sun and then rotate with time to the west of it.

However, a more accurate method of determining whether a CME will hit or miss Earth can be applied to SMEI sky map data once they are calibrated and largely free of instrument defects. These techniques formalize the earlier analyses of IPS and *Helios* photometer data and apply computer assisted tomography methods to data obtained from one location in space to provide CME distance from Earth. An early corotational technique that is still used (e.g., Altrock *et al.*, 1996) assumes that all material lies at the point of closest approach of the line of sight to the Sun. The daily observational brightness changes assumed at the limb show the location of the major coronal structures during a 27-day solar rotation interval. A corotational tomographic analysis (Jackson *et al.*, 1998; Kojima *et al.*, 1998; Jackson and Hick, 2002) improves upon this by making no *a priori* assumption about line of sight distribution of the material and iterates to determine a solution to a global solar wind model that fits observations.

More recently a time-dependent three-dimensional (3D) reconstruction technique, an enhanced version of this earlier tomographic analysis, has been developed (Jackson, Hick, and Buffington, 2002, and references therein), in which perspective views from a single point in space relax the assumption that heliospheric structures co-rotate and remain constant over time. In this newest time-dependent technique, a global kinematic solar wind model is formed at regular time intervals to fit observations covering a large range of solar elongations. These analyses allow short temporal variations in the solar wind such as CME disturbances to be reconstructed. In this technique the changing perspective views of the reconstructed solar wind comes primarily from the outward motion of solar wind plasma, and not solar rotation. This 3D reconstruction technique, originally designed to analyze IPS data, has been shown to work as well or better with *Helios* white light photometer data (Jackson and Hick, 2004).

Unlike ground-based interplanetary scintillation measurements, heliospheric brightness is only a tiny component of the night sky background brightness. Because the heliospheric time series signal is inseparable from the very bright zodiacal light component, except by its rapid (less than ~ 10 -day) variation over time, the 3D reconstruction analysis must deal with a steady background Thomson-scattering signal component as well as the time-varying one. Several techniques have been devised to include an estimate of this background signal in our Thomson-scattering analysis. In the current analysis an r^{-P} density profile with a constant value at 1 AU is added to the model data prior to the analysis. The sum of the modeled background brightness and the observed variable component relative to a mean is compared with total modeled brightness from the three-dimensional model. As with *Helios* we compare *in situ* densities over the time interval in question at Earth

with the densities derived by our model using SMEI data in order to provide a best interval fit to the value of P and the total density at 1 AU.

Once a three-dimensional result is available, it can be viewed from any perspective or extrapolated to any position in space. The most accurate locations in the reconstruction are where data coverage is most complete with the greatest signal relative to the many sources of observational noise, and this is usually at the observer's location. Current results of these 3D reconstruction analyses, are available as images using near real-time IPS observations as well as archival *Helios* analyses (Jackson and Hick, 2004).

To analyze SMEI sky maps and provide the highest 3D resolution, these analyses will require a computer system that not only includes most of the 40,000 lines of sight in the sky (from each unique 1° uncontaminated sky map resolution element present in a single sky map) from SMEI each 102 min orbit, but that will also involve 3D-MHD modeling in iterative steps rather than the kinematic model currently used as a kernel in the current 3D reconstruction.

4.4. SMEI DATA PRODUCTS

For the first three years of operation, SMEI data will be released for public distribution by the Air Force, and it is expected that this policy will remain in place for the life of the SMEI instrument. SMEI instrument data products have been made available at several locations by SMEI team members. The SMEI instrument produces approximately 3 gigabytes of data per day in normal mode operation as four-second data frames from the three SMEI cameras (Figure 6a). These data are archived at Hanscom AFB and disseminated to Sacramento Peak Observatory, the University of Birmingham, England, and UCSD.

AFRL, Hanscom has a website describing the SMEI instrument: <http://www.vs.afrl.af.mil/Division/VSBX/smei.html>. The official SMEI website providing SMEI sky map access is: <http://smei.nso.edu/>. This latter website provides SMEI data products using current Hanscom imaging processing techniques, and includes near real time SMEI Hammer–Aitoff sky map images, running difference sky maps, and sky maps that have been produced by removing some of the known long-term heliospheric features. This presentation now includes real-time maps in celestial coordinates. A movie loop that provides a running update of the last several days of SMEI skymaps in the modes mentioned above is also available on this website. Individual SMEI sky maps by orbit are archived on this website. Additional SMEI data products available to SMEI Team members and those associated with the project include these same maps in fisheye format and other data such as statistical information about the SMEI data processing of each orbit. In addition, each CME observed in the Hanscom processed sky maps (over 100 CMEs from the first year of data) are tabulated and measured in plane-of-sky coordinates and available to SMEI team members and associates.

Both the University of Birmingham and UCSD have web sites showing samples of the SMEI analysis. At the University of Birmingham, this site is: <http://www.sr.bham.ac.uk/~mpc/p2/smei/> and contains real-time information about the SMEI state of health as well as an archive of sky map images from the Hanscom-processed data. At UCSD the website used to display SMEI analysis progress and data products is: http://cassfos02.ucsd.edu/solar/smei_new/smei.html. This website provides samples of the UCSD sky map processing and other UCSD SMEI data products including preliminary tomographic reconstructions from small portions of the UCSD SMEI sky map analysis. UCSD maintains links from this website to a UCSD computer server that holds the complete archived SMEI image frame data set available via password access. Copies of these (Level 1A) data are also transferred onto DVDs at UCSD as soon as they are distributed by Hanscom. Portions of the programs allowing access and manipulation of these data sets and the manipulation of SMEI skymaps are available either as downloads from the UCSD website or, in the case of the Interactive Data Language (IDL) programming, as distributed SolarSoftware (SSW, Freeland and Handy, 1998).

5. Other Phenomena Observable by SMEI

5.1. BACKGROUND SIDEREAL SIGNALS

To provide accurate (0.1%) long-term photometry at the limiting resolution of SMEI, the shape of the point spread function (Figure 9) needs to be determined and incorporated into the analysis. Throughout the year, the scan of the instrument changes direction over a given portion of the sidereal sky. This causes the orientation of the point spread function to change significantly relative to other objects in the sidereal sky; thus the brightness of any point in the sky is influenced at different times of the year by varying amounts due to nearby slowly-evolving background stellar signals. Depending on the proximity of nearby sources, adjacent point sources limit the brightness determination of a given point in the sky beyond simple statistical noise, stray light and heliospheric brightness fluctuations. As mentioned previously, a stellar signal occupies about 200 SMEI CCD pixels, or about 1/2 square degree. The 60° SMEI data frame fills the 1242 active pixel length of the CCD, thus giving a SMEI plate scale of approximately 20 CCD pixels per degree across the sky in this dimension, but this varies with distance from the center of the data frame. A value close to 18 pixels per degree is more accurate in the data frame small dimension.

Stellar signals available photometrically from SMEI are of interest to astronomers. The regular 102 min cadence of stellar brightness measurements should yield refined light curves for ~1000 known variable stars and eclipsing binaries. Additional search studies of point source variability will also be important and include the following:

- Observations of novae.
- Stars with planets that transit across their disks causing characteristic light decreases.
- Brightness increases from gamma ray bursters.

5.2. ZODIACAL LIGHT AND THE GEGENSCHNITT

The *Helios* spacecraft have provided a zodiacal light model and test of its variation for SMEI. A hypothetical small variation in the zodiacal cloud spatial scale (mottling) or temporal scale could mask the signals of interplanetary structures, and the *Helios* data placed an upper limit on these variations of approximately 1 S10 unit. We presume that at the spatial and temporal scales of heliospheric brightness changes, the zodiacal cloud remains smooth and temporally non-varying even below this level. Gegenschein, thought to be due to backscatter from the zodiacal cloud, is present in the direction opposite the Sun at a level of about 200 S10 units. The Gegenschein is discernible even in SMEI first light sky maps, and we expect that results from ground-based observations (e.g., Hong *et al.*, 1985) will be improved significantly by these new space-based data.

Studies of zodiacal cloud temporal and spatial variations at the SMEI detection limit are also of interest. Replenishment of zodiacal dust must occur continuously because of the spiraling of small dust particles into the Sun (Poynting–Robertson effect) where they evaporate. The extent that comets replenish the zodiacal cloud is unknown, and may be factors of several below the full replenishment rate (Leinert and Grün, 1990). Thus, additional transient sources of dust replenishment have been postulated such as asteroid collisions. These might be observed by SMEI. The extent to which comets and asteroids have associated dust trails (Leinert and Grün, 1990) may also be constrained by SMEI observations. Views of these dust trails over time will show their three-dimensional locations.

5.3. COMETS

SMEI will view comets and determine their brightness distributions over large sky angles to faint levels. These measurements include the replenishment contributions to the zodiacal cloud as well as possible comet dust trails as mentioned above. Transient comet dust changes caused by comet breakup or comet nucleus rotation will be monitored with unprecedented regularity and precision. Comet gas trails will also be observed to the level of the zodiacal cloud brightness. In addition, a comet shock was remotely sensed in front of Comet West [1976b] (Jackson and Benensohn, 1990) by the *Helios* photometers. If a comet shock is viewed by the SMEI instrument, measurements of the placement of this shock relative to its nucleus will provide information about the comet volatile expulsion mechanism and comet composition.

5.4. AURORAL LIGHT

Light from auroras has been reported by Shuttle astronauts as high as 1000 km above the surface of the Earth on rare occasions (George Carruthers, private communication, 1991). From these observations and known auroral processes, Jackson *et al.* (1992) estimated that auroral brightness above 800 km could occasionally become greater than ~ 1 S10. SMEI has observed possible auroral light during periods of enhanced geomagnetic activity. During storm periods, such as in 29–30 May, 2003, these signals can be brighter than 200 S10. The frequency and brightness of this phenomenon were unexpected in SMEI observations. More recent observations, both space and ground-based (Romick *et al.*, 1999; Hunten, 2003), indicate that bright auroras from resonance scattering by the sunlit N_2^+ ion can be observed to heights as great as 1100 km. Views of auroras and their temporal changes can complement ground-based observations of this terrestrial phenomenon. Light this bright over time intervals short relative to the passage of a CME interferes with observations of heliospheric Thomson scattered light. This auroral light is often structured, and the implication from this is that this source of light is not located at the spacecraft but hundreds of km from it. Although this light can sometimes be a source of interference for SMEI in the darkest parts of the heliosphere and at specific positions relative to Earth's geomagnetic equator, the SMEI observations will provide new insight into this phenomenon.

5.5. THE GEOCORONA

The geocorona has been detected at various wavelengths, but especially in hydrogen Lyman- α radiation as a glow in the direction towards the Sun (Meier and Mange, 1973). Typical brightness of the geocorona in Balmer- α emission (6563 Å) is known to be as great as ~ 2.0 S10 units. The brightness fall-off with height above the surface of the Earth is unlike that of the aurora in that the geocorona is brightest at heights ≥ 100 km. This emission can contribute a background comparable to electron Thomson-scattering brightness observed by SMEI at 90° elongation and greater. However, to first order the geocorona remains approximately constant relative to solar elongation and is brightest towards and to the west of the Sun (Anderson *et al.*, 1987). The relative invariability of the geocorona at a given solar elongation on the time scales of mass ejections implies that this source of brightness should pose little problem for an Earth-orbit imager, but it might be possible to detect and monitor the geocoronal shape and overall asymmetry variation.

5.6. RAM GLOW AND OTHER SPACECRAFT-PRODUCED ILLUMINATION

Ram glow is a low-level light source that forms a comet-like halo and tail near a spacecraft in low-Earth orbit. The glow is caused by many different sources

(Torr, 1988), including a concentration of the ambient gases which peak in the ram direction, outgassing from the spacecraft, leakage, venting and thruster firings. The amounts of this glow vary from spacecraft to spacecraft. From Space Shuttle measurements at heights below 400 km some of the constituent molecular glows from atmospheric oxygen are significantly above the ~ 100 S10 unit zodiacal light background at 90° elongation. If the source of this light were to vary, it could cause significant problems for an imager at these heights; this dictated a SMEI launch to its present relatively high (840 km) orbit. With the possible exception of sources on the vehicle such as emissions from other experiments and the spacecraft itself, these sources of light extrapolate to well below the level that could cause a detrimental effect on the imager at the 840 km Coriolis orbit.

Dust particles from the Coriolis spacecraft can also occasionally cause potential unwanted noise in the CCD data frames. This unwanted noise will be present only if the particle is illuminated by sunlight and it is present in one of the SMEI camera fields of view. Because of the large SMEI point spread function, these particles, if they are more than a few meters from the instrument, will be difficult to distinguish from more distant orbiting spacecraft and space debris.

5.7. NEAR EARTH ASTEROIDS

Near-Earth asteroids can be detected by their gradual motion in the SMEI field of view from one orbit to the next. Jackson *et al.* (1994) predict a SMEI detection rate of 10–100 per year for a subclass of these objects brighter than 10th magnitude in the range of 13 m radius and above. More recent measurements of numbers of smaller objects in the range of 100–200 m radius are given by Morbidelli *et al.* (2002). Although these objects are larger than those SMEI can detect easily, extrapolating the size distribution derived from these measurements indicates that the lower bound given in the Jackson *et al.* (1994) estimate is more nearly correct. To be detected, these objects will require specialized analysis programs that are able to distinguish the relatively linear motion of these objects from one SMEI orbit to the next. This motion will need to be distinguished from chance linear associations from other transient point light sources such as variable stars.

6. Conclusion

SMEI was launched on 6 January 2003 and is providing images of the whole sky each orbit. Many CMEs have been observed in the SMEI data and are traced moving outward to beyond 1 AU. Results from the *Helios* photometers and from initial SMEI analyses demonstrate that the SMEI concept will work to map these data photometrically, and yield tomographic analyses of the Earth distance to these structures.

SMEI data are expected to improve the forecast capability for heliospheric structure arrival at Earth significantly since they permit accurate measurement of brightness in linear relationship to heliospheric density from nearly every location in the sky around Earth.

Acknowledgements

The work of B.V. Jackson, P.P. Hick and A. Buffington was supported in part at UCSD by AFRL contract AF19628-00-C-0029, AFOSR contract AF49620-01-1-0054, and NASA grant NAG5-134543. D. F. Webb, T. Kuchar and D. Mizuno were supported in part by AF19628-00-C-0073. The work of S. J. Tappin was partially supported under contract F61775-02-WE043 to the University of Birmingham. Computational facilities at the University of Birmingham are supported by STARLINK.

Appendix A: UCSD Image Processing

The UCSD image processing consists of a series of procedures that perform quality checks on the data, correct the data for instrumental and non-heliosphere effects, and create all-sky image maps for each orbit. The end product is a set of sidereal sky map images in R.A. and Dec. coordinates that can be combined and filtered to suit the user. This processing, that incorporates 32-bit PC technology and Fortran, C⁺⁺, and Interactive Data Language (IDL) programming, has been used in selected days-long SMEI data frame sequences from all cameras to provide sky maps from one day's worth of data from one camera in about one day.

A.1. DATA FRAME CONDITIONING

The basic steps needed to condition SMEI data in the UCSD processing system are as follows:

1. *Telemetry errors*: Checks of individual SMEI data frames show that they sometimes retain telemetry and other errors. Individual frames that are determined bad by anomalous values of frame pedestal and dark current are removed from further analysis consideration.
2. *Pixel pattern removal*: A pixel pattern (including hot pixels) is determined from weekly on-orbit calibrations. This pattern is subtracted from each SMEI data frame.
3. *Dark offset removal*: The bias and dark current are computed from empty and covered pixels on the data frame and subtracted from the data.
4. *Particle hit removal*: Pixels with anomalously high values are detected above the response of their neighboring 8 adjacent pixels, and not used in further analysis. The threshold is set sufficiently high so that the algorithm does not

- trigger significantly on stars as they move across the sequence of data frames. This algorithm saturates when particle hits are too numerous (see below).
5. *Saturation detection*: Excessive pixel-to-pixel response variation indicates large numbers of particle hits. This criterion removes whole data frames from further analysis.
 6. *Large scale flatfields*: UCSD flatfields from ground-based analysis are applied.
 7. *Geometric corrections*: Focal plane geometric projection effects are applied (see main text).
 8. *Excessive time-gradient detection*: Frames whose average response differs by more than 6 ADU from the average for this place in the orbit over several previous orbits minimum are discarded.
 9. *Imposition of the photometric field of view*: Only the photometric center portion of the illuminated field of the CCD is used for the photometric sky maps. This region is determined by two arcs with radii set so that only the photometric flat region of the CCD data frame is used in the analysis. The width of this region is approximately 3° .

A.2. SKY MAP CONSTRUCTION

We first construct a high-resolution seamless all-sky average map by combining and averaging SMEI data frames for each orbit into a single map in sidereal coordinates. This map is then re-sampled onto a lower-resolution set of rectangular sidereal right ascension and declination sky map images.

We use a Hierarchical Triangular Mesh (HTM) grid (Kunszt, Szalay, and Thakar, 2001) high-resolution mapping technique that averages SMEI data frames onto a seamless spherical sidereal coordinate map. This mapping, subdivides spherical octants into 11 triangle indexing levels which reach ~ 1 arc min ($\pm 0.015^\circ$ resolution) and allows reconstruction of the SMEI data frames so that bright star placements in them do not jeopardize the SMEI photometry in the 4×4 binned data. Higher-resolution engineering mode (or 1×1 binned data) require one further triangle index level to retain precise stellar locations in the map.

A lower-resolution (0.2°) sidereal map image in right ascension and declination coordinates is extracted for each orbit from the HTM grid. This lower-resolution image retains the original SMEI data frame resolution as well as the orientation of the asymmetric stellar point spread function, and is stored for further use. At this point in the analysis UCSD has shown that these sky map images can be averaged over up to several days time and subtracted from individual sky maps. For displays at the requisite SMEI photometric precision at 90° elongation, these sidereal sky maps are filtered with a circular Gaussian filter with an $1/e$ distance of 0.5° . Sky map images in other coordinates such as Sun-centered Hammer–Aitoff and fisheye sky maps as shown in Figure 7 are derived from these maps.

A.3. STAR REMOVAL

A sidereal R.A. and Dec. stellar catalog that has approximate “SMEI magnitudes” of ~ 5000 point sources (mostly stars) has been made available at UCSD to SMEI team members from different catalogs of bright objects. A standard stellar image shape similar to Figure 9 is formed by combining many bright-star sky-map images in the HTM grid map. Although not implemented in current difference sky map image analyses, this standard image and atlas, properly oriented for the particular orbit and normalized for a particular star’s brightness, has been demonstrated to subtract images so that the bright stars “disappear” from the low-resolution map. Each stellar brightness is multiplied by an ad hoc correction (near unity for most non-variable stars) such that each stellar response is subtracted from the sidereal map as determined by casting a circular mask around the sidereal location of that star and re-imaging it onto the lower-resolution sidereal map. Corrections and apparent brightness for each of these bright stars are retained for further study on each orbit. Down to the SMEI photometric limit, removing stars fainter than these need not retain knowledge of the asymmetric shape of the non-circular stellar point spread function. The remainder of these sky maps, derived from on-orbit data, will then be used for subtraction from the lower-resolution sidereal map. In future analyses to remove sidereal background over a larger time span than several days of orbit-to-orbit subtraction (Section 4.3), we intend to employ a two-step process which first removes bright stars and then the remaining residue.

Appendix B: AFRL Pipeline Processing

The AFRL pipeline (composite image) processing consists of a series of procedures that ingests the telemetry data, performs quality checks on the data, corrects the data for various instrumental and external effects, and creates several all-sky images for each orbit. The end product is a set of five Hammer–Aitoff images created for each orbit: an image derived from weighted input values, a FITS plane of the weights, an image of the observed sky using all the data, the same image using only “good” data, and a fifth image from which the stellar and zodiacal contents have been subtracted. The pipeline is able to process a day’s worth of data in less than a day.

B.1. DATA FRAME CONDITIONING

The basic corrections to the data in the pipeline processing are as follows:

1. *Rice-corrupted pixels*: Up to four of the final pixels in the data stream for a frame may be corrupted by the Rice compression. These pixels are removed from consideration.

2. *Bad pixel mask*: A bad pixel mask is determined from weekly on-orbit calibrations. Approximately one third of the pixels in camera 3 are identified as “hot” or “flipper” pixels due to the elevated focal plane temperatures. These pixels are omitted from further processing.
3. *Moon and planet detection*: Entire frames contaminated by the Moon and Venus are flagged as bad so that they can be discarded.
4. *Saturation detection*: Regions of excessive pixel saturations and anomalously elevated levels are checked and affected frames are flagged as bad so that they can be discarded.
5. *Position tagging*: The pixels are assigned right ascension and declination coordinates.
6. *Dark offset removal*: The bias and dark charge are computed from the appropriate columns and removed from the data.
7. *Spike detection and removal*: Pixels with locally anomalously high values are detected and flagged in a bad pixel mask applied to each frame.
8. *Large scale flatfields*: UCSD flatfields are applied.
9. *On-board flat-field equalization*: Frames that have not been flat-fielded on-board the spacecraft are multiplied by 0.75 to make them consistent with data frame levels where on board flat fields have been applied.
10. *Geometric corrections*: Focal plane projection effects as described by UCSD are applied.
11. *Excessive median-gradient detection*: Normally the median of the response distribution does not increase by more than about 1 ADU from frame to frame for a given camera. Frames whose median increases by more than 10 ADU from the previous frame are flagged as bad so that they can be discarded.
12. *Sub-sampling the focal plane*: Only half (2.5°) of the data from the 5° -wide in-scan field of regard of the CCD that is transmitted from the focal plane is used in the imaging. The accepted data were identified by the UCSD flat field corrections.

B.2. IMAGE CONSTRUCTION

We first construct a relatively high-resolution all-sky map image from the position tagged data, for each orbit, in a fixed projection that (ideally) would have no preferred direction. This image is then re-sampled onto the (lower resolution) Sun-centered Hammer–Aitoff projection. An advantage to this approach is that we can easily re-project the higher resolution image created from given orbit into different representations since the re-sampling is a faster operation than the basic image construction. This is useful, for example, in using difference images between successive orbits to identify transient phenomena such as CMEs, as we can always make two orbits in the same sidereal projection, which is necessary to remove stars in the difference image.

We use the COBE Quadrilateralized Spherical Cube (CSC) (Calabretta and Greisen, 2002 defined the CSC FITS standard) for the high-resolution fixed projection images. This is a projection in which the sky is divided into six flat square faces. The projection for each face is designed such that the distortion and deviations from the pixel equal-area condition are minimized. The 12 arc min (0.2°) pixel size of the SMEI science data is adopted for the pixel size in these high-resolution images.

As may be seen in Figure 9, the point response function is quite asymmetric especially in the in-scan direction. Since the 1° program requirement for resolution allows us to smooth the data, we use the transpose of the point response function to smooth the data while projecting it onto the COBE cube. Such smoothing of the data produces an ovoid shape for the point response function with axis of about $1^\circ \times 0.5^\circ$ in the in-scan and cross-scan directions, respectively. The transpose response function is smoothed with a 0.9° box averaging in the cross-scan direction such that the point response function is circularly symmetric after the filter function is applied to the data. The filter function is centered on each of the COBE cube pixels and the observations immediately around that point are averaged with weights defined by the filter function. Thus, the transpose plus cross-scan averaged filter function not only smooths the data but projects it on the proper grid.

A Hammer–Aitoff image is created for each orbit with the Sun at the center of the image. We select a 0.5° pixel for the Hammer–Aitoff images, as this is the Nyquist sampling interval for 1° resolution specified by the program. The ecliptic coordinates of the Sun are rounded to the nearest integer and the data is projected onto the Hammer–Aitoff image with 0.5° pixel spacing using a smoothing filter.

The final Hammer–Aitoff files contain 5 image planes: the “weighted data” and “weights” planes for the “good data” only (these planes are the actual products of the image construction process), the “good data” and “all data” images in true sky values (dividing the weighted-data plane by the weights plane), and the background subtracted image.

B.3. GALACTIC BACKGROUND SUBTRACTION

Camera 1 and 2 measurements were obtained from orbits sampled approximately every 10 days over a 108-day period. The observations were filtered with the modified transpose of the point response function and imaged onto a COBE-cube. The major planets have also been removed by excising a small box around them. After removal of the zodiacal light model, the processed images are averaged together. The result is a COBE-cube representation of the sidereal sky. This image is subtracted from each COBE image for a single orbit and the result is re-gridded to the Sun-centered Hammer–Aitoff projection.

B.4. ZODIACAL BACKGROUND

The zodiacal module of the Celestial Background Scene Descriptor (CBZODY 6 – Noah and Noah, 2001) is used to compute the zodiacal background. The module includes a modified form of the Reach, Franz, and Weiland (1997) dust bands component, which was found to predict too much infrared flux at smaller elongations (Price *et al.*, 2003) and in the SMEI observations. Thus, only the cloud component is used. The zodiacal model is computed at the pixel centers of the Sun-centered Hammer–Aitoff projection for a given orbit, rather than the COBE cube, as the scale lengths for this phenomenon are large and this significantly improves the speed of calculation. Since the predicted zodiacal image is computed in units of MJy sr⁻¹, the best fit scaling between the model and observations provides an initial calibration, 1 MJy sr⁻¹ = 1250 ADU.

References

- Allen, C. W.: 2000, *Allen's Astrophysical Quantities*, Springer-Verlag, New York.
- Altrock, R. C., Hick, P., Jackson, B. V., Hoeksema, J. T., Zhao, X. P., Slater, G., and Henry, T. W.: 1996, *Adv. Space Res.* **17**(4/5), 235.
- Ananthakrishnan, S., Coles, W. A., and Kaufman, J. J.: 1980, *J. Geophys. Res.* **85**, 6025.
- Anderson, D. E., Jr., Meier, R. R., Hodges, R. R., Jr., and Tinsley, B. A.: 1987, *J. Geophys. Res.* **92**, 7619.
- Biretta, J. A. and Lubin, L. M., (eds.): 2002, *Wide Field and Planetary Camera 2 Instrument Handbook*, ver. 7, Baltimore, STSCI, p. 99.
- Brueckner, G. E., Howard, R. A., Koomen, M. J., Korendyke, C. M., Michels, D. J., Moses, J. D., Socker, D. G., Dere, K. P., Lamy, P. L., Llebaria, A., Bout, M. V., Schwenn, R., Simnett, G. M., Bedford, D. K., and Eyles, C. J.: 1995, *Solar Phys.* **162**, 357.
- Behannon, K. W., Burlaga, L. F., and Hewish, A.: 1991, *J. Geophys. Res.* **96**, 21,213.
- Buffington, A., Booth, C. H., and Hudson, H. S., 1991, *Publ. Astr. Soc. Pac.* **103**, 685.
- Buffington, A., Jackson, B. V., and Hick, P. P.: 2002, in *S.P.I.E. proc.* **4853**, 490.
- Calabretta, M. and Greisen, E. W.: 2002, *Astron. Astrophys.* **395**, 1077.
- Coles, W. A. and Kaufman, J. J.: 1978, *Radio Sci.* **13**, 591.
- Chapman, R. W.: 1979, *Sky and Telescope* **58**, 223.
- Eyles, C. J., Simnett, G. M., Cooke, M. P., Jackson, B. V., Buffington, A., Hick, P. P., Waltham, N. R., King, J. M., Anderson, P. A., and Holladay, P. E.: 2003, *Solar Phys.* **217**, 319.
- Freeland, S. L. and Handy, B. N.: 1998, *Solar Phys.* **182**, 497.
- Gaiser, P. W.: 1999, *IEEE International Microwave Symposium Digest 1*, Piscataway, N. J., p. 408.
- Gapper, G. R., Hewish, A., Purvis, A., and Duffet-Smith, P. J.: 1982, *Nature* **296**, 633.
- Garcia, F. J., Taylor, M. J., and Kelley, M. C.: 1997, *Applied Optics* **36**, 7374.
- Hewish, A. and Bravo, S.: 1986, *Solar Phys.* **106**, 185.
- Hewish, A., Scott, P. F., and Wills, D.: 1964, *Nature* **203**, 1214.
- Hong, S. S., Misconi, N. Y., van Dijk, M. H. H., Weinberg, J. L., and Toller, G. N.: 1985, in R. H. Giese and P. Lamy (eds.), *Proc. Properties and Interactions of Interplanetary Dust* (Reidel, Dordrecht), p. 33.
- Hunten, D. M.: 2003, *Planetary Space Sci.* **51**, 887.
- Jackson, B. V.: 1985, *Solar Phys.* **100**, 563.

- Jackson, B. V.: 1986, *Adv. Space Res.* **6**, 307.
- Jackson, B. V.: 1991, *J. Geophys. Res.* **96**, 11307.
- Jackson, B. V. and Benensohn, R. M.: 1990, *Earth, Moon, Planets* **48**, 139.
- Jackson, B. V. and Hick, P. P.: 2002, *Solar Phys.* **211**, 344.
- Jackson, B. V. and Hick, P. P.: 2004, in Gary, D. E., and Keller, Ch.O. (eds.), *Solar and Space Weather Radiophysics*, Kluwer ASSL **314**, 353.
- Jackson, B., Gold, R., and Altrock, R.: 1991, *Adv. Space Res.* **11**, 377.
- Jackson, B. V., Hick, P. P., and Buffington, A.: 2002, in *SPIE Proc.* **4853**, 23.
- Jackson, B. V., Hudson, H. S., Nichols, J. D., and Gold, R. E.: 1989, in *Solar System Plasma Physics*, Waite, J. H., Jr, Burch, J. L., and Moore, R. L. (eds.), *Geophysical Monograph* **54**, 291.
- Jackson, B. V., Webb, D. F., Altrock, R. C., and Gold, R.: 1992, in *Eruptive Solar Flares*, Svestka, Z., Jackson, B. V., and Machado, M. E. (eds.), Springer-Verlag, Heidelberg, 322.
- Jackson, B. V., Buffington, A., Hick, P., Kahler, S. W., and Webb, D. F.: 1994, *Astron. Astrophys. Suppl. Ser.* **108**, 279.
- Jackson, B. V., Buffington, A., Hick, P., Kahler, S. W., Keil, S. L., Altrock, R. C., Simnett, G. M., and Webb, D. F.: 1997, *Phys. Chem. Earth* **22**, 441.
- Jackson, B. V., Hick, P.L., Kojima, M., and Yokobe, A.: 1998, *J. Geophys. Res.* **103**, 12,049.
- James, J. F., Mukai, T., Watanabe, T., Ishigura, M., and Nakamura, R.: 1997, *Monthly Notices Royal Astron. Soc.* **288**, 1022.
- Keil, S. L., Altrock, R. C., Kahler, S., Jackson, B. V., Buffington, A., Hick, P. L., Simnett, G. M., Eyles, C. J., Webb, D., and Anderson, P.: 1996, *SPIE Proc.* **2804**, 78.
- Kojima, M. and Kakinuma, T.: 1990, *Space Sci. Rev.* **53**, 173.
- Kojima, M., Tokumaru, M., Watanabe, H., Yokobe, A., Asai, K., Jackson, B. V., and Hick, P. L.: 1998, *J. Geophys. Res.* **103**, 1981.
- Kunszt, P. Z., Szalay, A. S., and Thakar, A. R., 2001, in Garching, Banday, Zaroubi, and Bartelmann, (eds.), *Mining the Sky: Proceedings of the MPA/ESO/MPE Workshop*, Springer-Verlag, Berlin, p. 631.
- Leinert, C. and Grün, E.: 1990, in Schwenn, R. and Marsch, E. (eds.), *Physics of the Inner Heliosphere 1*, Springer-Verlag, Berlin, 207.
- Leinert, C., Link, H., and Salm, N.: 1981, *J. Space Sci. Instr.* **5**, 257.
- Leinert, C., Link, H., Pitz, E., Salm, N., and Knuppelberg, D.: 1975, *Raumfahrtforschung* **19**, 264.
- MacQueen, R. M., Csoeke-Poeckh, A., Hildner, E., House, L., Reynolds, R., Stanger, A., Tepoel, H., and Wagner, W.: 1980, *Solar Phys.* **65**, 91.
- Martin Marietta Company: 1977, *SPIE Proc.* **107**, 168.
- Meier, R. R. and Mange, P.: 1973, *Planet. Space Sci.* **21**, 309.
- Morbidelli, A., Jedicke, R., Bottke, W. F., Michel, P., and Tedesco, E. F.: 2002, *Icarus*, **158**, 329.
- Noah, P. V. and Noah, M. A.: 2001, in *Validation Report for the Celestial Background Scene Descriptor (CBSD) Zodiacal Emission (CBZODY6) Model*, AFRL-TR-2001-1578.
- Price, S. D., Noah, P. V., Mizuno, D., Walker, R. G., and Jayaraman, S.: 2003, *Astron. J.* **125**, 962.
- Reach, W. T., Franz, B. A., and Weiland, J. L.: 1997, *Icarus* **127**, 461.
- Richter, I., Leinert, C., and Planck, B.: 1982, *Astron. Astrophys.* **110**, 115.
- Romick, G. J., Yee, J-H., Morgan, M. F., Morrison, D., Paxton, L. J., and Meng, C-I.: 1999, *Geophys. Res. Lett.* **26**, No. 7, 1003.
- Sheeley, N. R., Jr, Michels, D. J., Howard, R. A., and Koomen, M. J.: 1980, *Astrophys. J.* **237**, L99.
- Tappin, S. J., Buffington, A., Cooke, M. P., Eyles, C. J., Hick, P. P., Holladay, P. E., Jackson, B. V., Johnston, J. C., Kuchar, T., Mizuno, D., Mozer, J. B., Price, S., Radick, R. R., Simnett, G. M., Sinclair, D., Waltham, N. R., and Webb, D. F., *Geophys. Res. Lett.* **31**, L02802.
- Torr, G.: 1988, *NASA Conference Publication 3002*.
- Webb, D. F., Johnston, J. C., and Radick, R. C.: 2002, *EOS, Transactions, American Geophys. Union* **83**, 33.